Journal of Applied Physics

RESEARCH ARTICLE | OCTOBER 20 2025

Low-frequency noise characteristics of waveguide-integrated lateral and vertical Ge-on-Si p–i–n photodiodes

Solomon Musibau ; Kellen P. Arnold ; Anurag R. Veluri ; Jacopo Franco ; Artemisia Tsiara ; Kristof Croes ; Joris Van Campenhout ; Ronald D. Schrimpf ; Robert A. Reed ; Ingrid De Wolf ; Daniel M. Fleetwood

Check for updates

J. Appl. Phys. 138, 155706 (2025)
https://doi.org/10.1063/5.0287589

CHORUS

View Online

Export Citation

Articles You May Be Interested In

Temperature dependence of the low-frequency noise in AlGaN/GaN fin field effect transistors

J. Appl. Phys. (October 2024)

Dark current analysis in high-speed germanium p-i-n waveguide photodetectors

J. Appl. Phys. (June 2016)

Analysis and modeling of the influence of gate leakage current on threshold voltage and subthreshold swing in p-GaN gate AlGaN/GaN high electron mobility transistors

J. Appl. Phys. (April 2024)

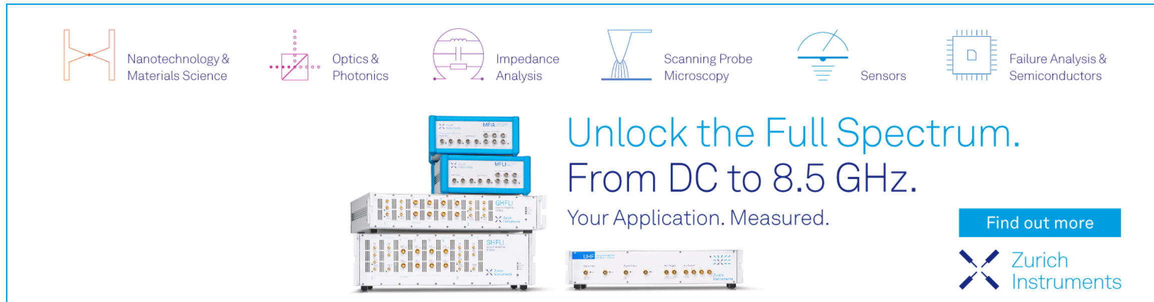

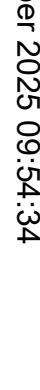

Journal of Applied Physics | ARTICLE | pubs.aip.org/aip/jap

Low-frequency noise characteristics of waveguide-integrated lateral and vertical Ge-on-Si p–i–n photodiodes

Cite as: J. Appl. Phys. **138**, 155706 (2025); doi: 10.1063/5.0287589
Submitted: 25 June 2025 · Accepted: 30 September 2025 ·
Published Online: 20 October 2025

Solomon Musibau,[1,2,a)] Kellen P. Arnold,[3] Anurag R. Veluri,[4] Jacopo Franco,[2] Artemisia Tsiara,[2] Kristof Croes,[2] Joris Van Campenhout,[2] Ronald D. Schrimpf,[3,4] Robert A. Reed,[3,4] Ingrid De Wolf,[1,2] and Daniel M. Fleetwood[3,4]

AFFILIATIONS

[1]Department of Materials Engineering, KU Leuven, Leuven 3001, Belgium
[2]imec, Leuven 3001, Belgium
[3]Interdisciplinary Materials Science Program, Vanderbilt University, Nashville, Tennessee 37235, USA
[4]Department of Electrical and Computer Engineering, Vanderbilt University, Nashville, Tennessee 37235, USA

[a)]**Author to whom correspondence should be addressed:** solomon.musibau@imec.be

19 December 2025 09:54:34

ABSTRACT

We report forward bias and temperature-dependent low-frequency (LF) noise characteristics of waveguide-integrated Ge-on-Si p–i–n photodiodes across three architectures: doped-Si lateral, doped-Ge and doped-Si lateral, and vertical heterojunctions. Forward I–V measurements and activation energy analysis reveal mixed Shockley–Read–Hall recombination and diffusion transport below 0.4 V, with transport ratios evolving more gradually with temperature in vertical devices than in lateral devices. At room temperature, the noise spectra exhibit broad generation-recombination (G–R) features near $V = 0.2\,\mathrm{V}$, aligning with the transition from G–R-dominated ($S_I \sim I^2$ for $V \leq 0.2\,\mathrm{V}$) to diffusion-limited ($S_I \sim I$ for $0.2\,\mathrm{V} \leq V \leq 0.5\,\mathrm{V}$) current noise. Technology computer-aided design simulations indicate that in lateral devices the defect-rich Ge/Si interface lies within the depletion region, where interface traps strongly enhance G–R noise. In vertical devices, the Ge/Si interface is located outside the depletion zone, so the noise response is dominated by bulk Ge traps. Temperature-dependent measurements reveal a smooth transition from G–R noise below 300 K to diffusion-type flicker noise at higher temperatures. Notably, normalized noise S_I/I^2 peaks around 300 K in lateral devices, marking a crossover in dominant noise mechanisms. Observed increases of low-temperature noise after total-ionizing-dose irradiation in lateral devices result from the electrostatic activation of traps within the narrow depletion region, whereas the increase of forward current originates mainly from radiation-induced additional leakage paths. These results establish LF noise spectroscopy as an effective tool for probing interfacial defect dynamics in Ge-on-Si photodiodes.

© 2025 Author(s). All article content, except where otherwise noted, is licensed under a Creative Commons Attribution (CC BY) license (https://creativecommons.org/licenses/by/4.0/). https://doi.org/10.1063/5.0287589

I. INTRODUCTION

Integrated silicon photonics has emerged as a transformative platform for next-generation optical communication, offering high bandwidth, energy efficiency, and dense integration compared to conventional electronic interconnects.[1–5] Within this ecosystem, waveguide-coupled germanium (Ge)-on-silicon (Si) p–i–n photodiodes (PDs) serve as critical components, enabling efficient optical-to-electrical signal conversion at telecommunication wavelengths.[6–11] Beyond terrestrial optical communication systems, Ge-on-Si photodiodes also hold promise for space applications.[12–15] However, the heterogeneous integration of germanium on silicon introduces material quality challenges that can compromise device performance and stability. The 4.2% lattice mismatch between Ge and Si introduces strain-induced interface defects and threading dislocations, while thermal budget constraints and oxide interface quality (Ge/SiO_2 and Si/SiO_2) can result in higher densities of

active trap centers inside and along active regions of devices.[16–19] These defects can lead to elevated dark current, degraded responsivity, and increased variability, ultimately limiting yield and long-term reliability.[20–24] With the growing deployment of advanced germanium-based photonic devices, such as GeSi electro-absorption modulators[25,26] and Ge-on-Si avalanche photodiodes,[27] the need for sensitive, non-destructive tools to diagnose defect properties becomes increasingly critical. Low-frequency (LF) $1/f$ noise spectroscopy is a powerful tool to study material quality, carrier trapping-detrapping kinetics, transport mechanisms, and reliability of opto-electronic devices.[28–38] Although extensive studies have characterized $1/f$ noise in Schottky diodes[39,40] and p–(i)–n junction-based devices,[41–49] the LF noise behavior of waveguide-integrated Ge-on-Si PDs remains largely unexplored, with prior work focusing only on reverse-bias conditions at room temperature.[50,51]

In this work, we present a comprehensive investigation of LF noise characteristics in waveguide-integrated Ge-on-Si p–i–n heterojunction photodiodes. We explore the noise properties within the forward conduction regime, where the sensitivity to traps is concentrated within narrow depletion regions. Particular attention is given to the structural differences between lateral and vertical junctions, where the defect-rich Ge/Si interface lies in different positions within the space-charge regions. We examine how the noise power spectral density evolves with forward voltage, temperature, and total-ionizing-dose (TID) exposure. Experimental measurements are complemented by calibrated Technology Computer-Aided Design (TCAD) simulations and established $1/f$ noise models for p–i–n junctions. Through this combined approach, we correlate the dominant noise mechanisms with the spatial locations of the generation-ecombination (G–R) centers and diffusion-related noise sources in the different photodiode geometries.

II. EXPERIMENTAL DETAILS

A. Materials

Waveguide-coupled Ge-on-Si p–i–n photodiodes were fabricated using imec's iSiPP50G 200 mm SOI platform, featuring a 220 nm Si layer on top of a 2μm buried oxide (BOX).[1] Three common Ge-on-Si photodiode architectures were investigated in this study: doped-Si lateral (SLPIN), doped-Ge and doped-Si lateral (SLPIN-D), and vertical (VPIN) p–i–n heterojunctions.[24] Figures 1(a)–1(c) illustrate the typical cross sections of these structures. Their respective device lengths are 20.8, 40.0, and 15.2μm. In the SLPIN-D devices, the presence of additional p^+ and n^+ Ge doping enhances the lateral junction electric field and, thus, improves the electro-optic bandwidth performance of the photodiodes. Additional information on the process flow is provided in previous studies.[1,52] The Ge layers were grown by selective epitaxy on Si, within shallow trench isolation (STI) SiO_2 oxide, resulting in a 4.2% lattice mismatch between materials. This mismatch can result in defects and strained-induced threading dislocations, especially near the Ge/Si interface. These defects are critical for low-frequency noise as they can act as G–R centers. Figure 1(d) depicts bright-field transmission electron microscopy (BF-TEM) cross-sectional images of a SLPIN device. A zoom near the Ge/Si interface regions reveals interface roughness and dislocations.

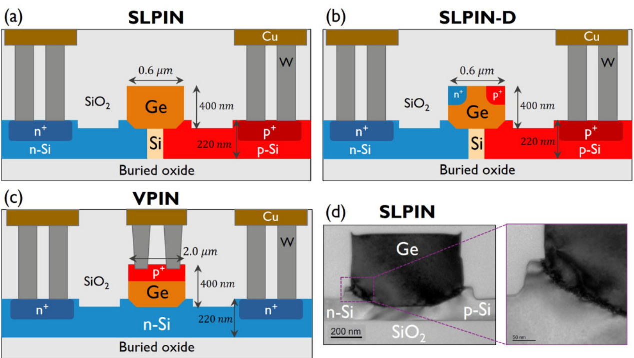

FIG. 1. Cross-sectional view of (a) doped-Si lateral (SLPIN), (b) doped-Ge and doped-Si lateral (SLPIN-D), and (c) vertical (VPIN) Ge-on-Si p–i–n photodiodes. (d) Bright-field transmission electron microscope (BF-TEM) images of the SLPIN device, including a zoom near the Ge/Si heterointerface. Interface roughness and threading dislocations within the Ge layer are visible.

B. Measurements

Current–voltage (I–V) measurements were conducted in the range of −1 to +1 V using an Agilent/Keysight 4156A semiconductor parameter analyzer under dark conditions. Low-frequency noise spectra were recorded as a function of applied voltage within the frequency range of 1–390 Hz and temperature range of 240–360 K. The voltage noise power spectral density, S_V, was measured across a low-noise load resistor R_L connected in series with the photodiodes.[53,54] The measurement setup included a low-noise voltage preamplifier (SR-560), a SR-760 FFT spectrum analyzer, and a cryostat-based system.[54,55] To ensure optimal noise measurement conditions, the value of the series load resistor was adjusted according to the bias current. The current noise spectral density, S_I, was extracted using the relation $S_I = S_V - S_{Vbcgr}[(R_L + R_d)/(R_L R_d)]^2/G^2$, where $R_d = (dI/dV)^{-1}$ is the differential resistance of the photodiode, G is the gain of the low-noise amplifier, and S_{Vbcgr} is the background noise measured at zero bias.[54] All measurements were carried out inside electromagnetic shielding to minimize interference from external noise sources. Each LF noise spectrum was post-processed to remove unwanted spikes originating from the 60-Hz power line interference and its associated harmonics. Random telegraph signal (RTS) measurements were performed using a Keysight E4727-A advanced low-frequency noise analyzer and a Keysight B1500A semiconductor parameter analyzer. For each device architecture, at least two nominally identical photodiodes were characterized. The devices showed consistent I–V characteristics and low-frequency noise spectra, with variations within typical device-to-device fluctuations and specifications. The data presented are representative of this reproducible behavior.

X-ray irradiation experiments were conducted at Vanderbilt University using a 10-keV ARACOR model 4100 x-ray irradiator, delivering a total-ionizing-dose of 1 Mrad (SiO_2) at a dose rate of 28.14 krad (SiO_2)/min.[56] During exposure, all device terminals were grounded to control fields and potential charging effects during exposure. Voltage- and temperature-dependent I–V and

19 December 2025 09:54:34

© Author(s) 2025

low-frequency noise measurements were performed approximately 24 h after irradiation. These experiments were limited to the SLPIN and SLPIN-D device configurations. Previous studies have shown that VPIN devices exhibit full recovery of TID-induced degradation within 24 h of irradiation, and VPIN devices were, therefore, excluded from post-irradiation characterization.[14]

III. SIMULATION DETAILS

The Synopsys Sentaurus TCAD (Technology Computer-Aided Design) simulator was employed to investigate the physical behavior of the space-charge region in various photodiode configurations. Following a previously established methodology,[24] 2D TCAD models were developed using the available design layout file, fabrication process data, and TEM images. The simulations numerically solve Poisson's equation and drift-diffusion transport equations for electrons and holes, incorporating Fermi–Dirac statistics and high-field saturation models for carrier mobility in both Si and Ge. Multiple recombination mechanisms are included, such as Shockley–Read–Hall (SRH), Auger, and field-enhanced Hurkx trap-assisted tunneling (TAT).[24] Temperature and doping dependencies were accounted for in all physical models. Trap energy levels, representing defect states located within the Ge bulk (due to threading dislocations) and at the Ge/Si, Ge/SiO_2, and Si/SiO_2 interfaces, were assumed to be at approximately midgap ($E_t = E_i$), constituting the most effective SRH recombination centers.[57] Simulation parameters were selected based on values reported in similar structures (see the supplementary material for a summary of the main TCAD parameters used for the Ge material).[24]

IV. RESULTS AND DISCUSSIONS

A. Current–voltage characteristics

Figures 2(a)–2(c) show the temperature-dependent *I*–*V* characteristics of the three Ge-on-Si photodiode configurations. Each device exhibits strong temperature dependence both in reverse and forward bias regimes. In the reverse-bias regime, we can identify the dominant charge transport mechanism by analyzing the temperature dependence of the dark current (I_{dark}) using the

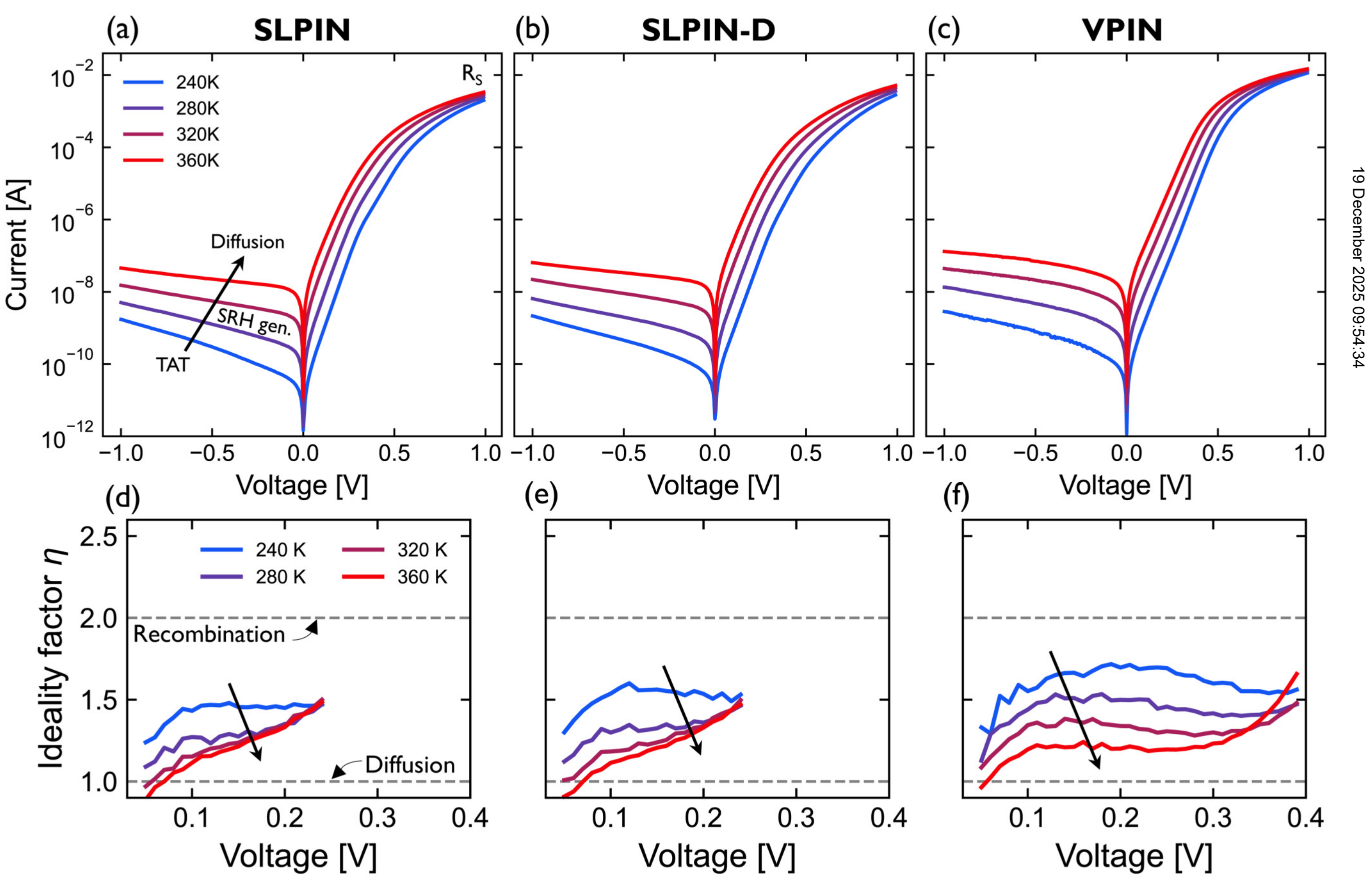

FIG. 2. Temperature-dependent *I*–*V* characteristics of the (a) SLPIN, (b) SLPIN-D, and (c) VPIN Ge-on-Si photodiodes. Temperature-dependent local ideality factor η as a function of forward voltage, computed from the *I*–*V* curves measured for the (d) SLPIN, (e) SLPIN-D, and (f) VPIN devices. The η plots are shown only for the voltage ranges where the η estimate remains valid.

19 December 2025 09:54:34

© Author(s) 2025

Arrhenius relation within each pair of consecutive temperatures,[58]

$$I_{dark} \propto \exp(-E_A/k_B T). \quad (1)$$

Here, E_A is the activation energy, k_B the Boltzmann constant, T the temperature, and q the elementary charge. Previous studies show that Ge-on-Si p–n and p–i–n junctions exhibit non-linear Arrhenius relations, indicating a strong evolution of the dominant conduction mechanism in function of voltage and temperature.[20,24,59,60] Typically, four main reverse leakage mechanisms are identified for these devices: (1) diffusion of minority carriers across the depletion region ($E_A = E_{g,Ge} = 0.66\,\text{eV}$), (2) SRH generation of electron–hole pairs via mid-bandgap traps within the depletion region ($E_A = E_{g,Ge}/2 = 0.33\,\text{eV}$), (3) field-enhanced Hurkx TAT ($0.1\,\text{eV} \leq E_A \leq 0.33\,\text{eV}$), and (4) band-to-band tunneling (BTBT, $E_A < 0.1\,\text{eV}$).[59] Consistent with previous observations,[20,24,60] the dominant conduction mechanism in our devices evolves gradually from TAT at high reverse voltages and low temperatures to minority carrier diffusion at lower reverse voltages and higher temperatures (see the supplementary material for the detailed E_A data). This behavior confirms the presence of pre-existing defects, situated within the depletion region and actively contributing to the measured I_{dark} for all photodiode configurations under study.

At high forward voltage (>0.6 V), device characteristics tend toward saturation, indicating that the contribution of the series resistance becomes increasingly dominant at higher voltages. At low injection levels (<0.5 V), a qualitative determination of dominant charge transport mechanisms in forward bias can be achieved by analyzing temperature-dependent *I*–*V* characteristics. Following the method proposed by Grushko *et al.*,[61] values of E_A, extracted in a specific temperature range, are plotted as a function of forward voltage alongside two theoretical boundaries: $E_{A1} = E_{g,Ge} - qV$ and $E_{A2} = \frac{1}{2}(E_{g,Ge} - qV)$, indicated by the dark lines in Fig. 3. The relative position of the experimental $E_A(V)$ with respect to the lines is used to determine the dominant current transport mechanism. Figure 3 shows the activation energy as a function of forward voltage for the three photodiode structures. Between 0 and 0.4 V, all three configurations exhibit mixed current transport dominated by SRH recombination in the space-charge region and carrier diffusion processes. Above 0.4 V, enhancement of majority carrier injection occurs across the junctions, and, thus, the current becomes dominated by a pure diffusion process.

Additionally, the diode ideality factor η can be used to identify the dominant carrier transport mechanisms under forward bias. Typically, an ideality factor of 1 is associated with a pure diffusion current due to recombination of carriers in the quasi-neutral regions. A value of 2 is associated with a pure SRH recombination current via traps localized inside the space-charge region.[57] To capture the local variations in conduction behavior across the forward bias range in complex heterojunctions, the use of local ideality factor η_i is more appropriate. η_i is extracted at each voltage step V_i using the following expression:[62]

$$\eta_i(V_i) = \frac{V_i - V_{i-1}}{\ln\left(I_i/I_{i-1}\right)\frac{k_B T}{q}}. \quad (2)$$

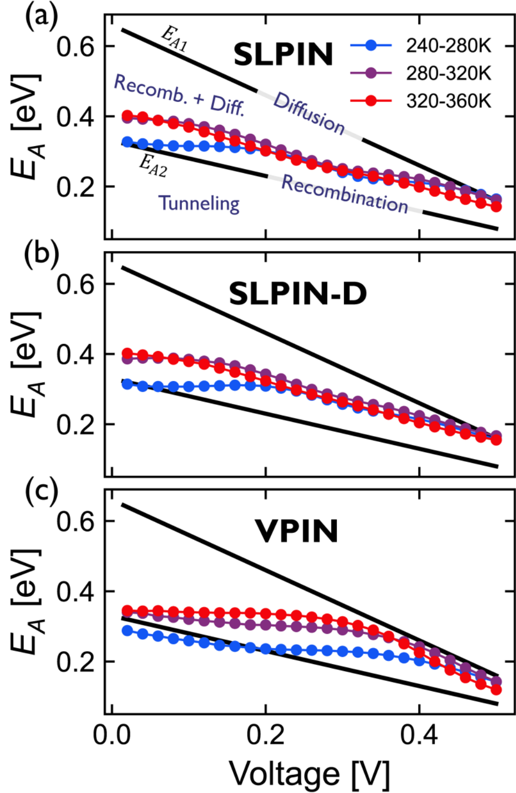

FIG. 3. Activation energy, E_A, as a function of the forward voltage, extracted across three different temperature range for (a) SLPIN, (b) SLPIN-D, and (c) VPIN devices. The dark lines, $E_{A1} = E_{g,Ge} - qV$ and $E_{A2} = \frac{1}{2}(E_{g,Ge} - qV)$, demarcate dominant conduction mechanisms.

This formulation assumes a moderate forward bias, for which the voltage drop across the series resistance, IR_s, remains negligible. To determine the applicable range for each photodiode, we compared the measured *I*–*V* characteristics with the ideal Shockley diode slope and identified the onset of deviation (see the supplementary material). The validity range of η_i extraction was found to differ across devices: $V < 0.25\,\text{V}$ for SLPIN/SLPIN-D and $V < 0.4\,\text{V}$ for VPIN devices. This difference results from the larger series resistance of the SLPIN ($R_s \approx 110\,\Omega$) and SLPIN-D ($R_s \approx 70\,\Omega$) devices compared to the VPIN devices ($R_s \approx 25\,\Omega$), which narrows the voltage window where the ideality factor remains unaffected by IR_s effects.

Figures 2(d)–2(f) show η_i as a function of V_i at temperatures ranging from 240 to 360 K. The lateral (SLPIN and SLPIN-D) and vertical (VPIN) configurations exhibit distinct ideality factor trends, reflecting their different heterojunction structures and carrier transport.[13] In all cases, a systematic decrease in the ideality factor is observed with increasing temperature, indicating a shift toward diffusion-dominated conduction at elevated temperatures. Across the entire temperature range, ideality factors remain between 1 and 2, consistent with a mixed transport regime where

19 December 2025 09:54:34

© Author(s) 2025

both diffusion and SRH recombination contribute to the forward current. However, at lower temperatures, the ideality factor approaches 2, emphasizing the stronger role of SRH recombination through interface and/or bulk traps under these conditions.

B. Voltage dependence of LF noise

To further study the recombination mechanisms identified by the I–V and E_A analysis, we employ LF noise spectroscopy. Noise measurements can be used as a complementary tool to probe carrier number fluctuations, providing additional information about the trap properties and their spatial location within the device. In particular, analyzing the voltage dependence of the LF noise allows us to decouple diffusion-related and G–R related fluctuations and to assess the relative role of interface and bulk defects in different device geometries.

While photodiodes generally operate in reverse bias, in this work, LF noise measurements were performed under forward bias. In reverse bias, the combination of very low dark currents (few nA to 100 nA) and large differential resistances R_d (MΩ – GΩ) makes the reliable extraction of S_I difficult in our setup. A careful balance between R_d and the load resistance R_L is essential to maintain high voltage-to-current noise conversion across the diode. Increasing R_L introduces additional thermal noise, which can dominate the intrinsic noise of the photodiode. From a physical perspective, recombination processes in forward bias are confined to a narrow depletion region (as confirmed below by simulations), offering a method to locally probe defect-related fluctuations within specific spatial regions. Under reverse bias, the same defects contribute through generation processes in an extended depletion region,[24] while additional SRH centers located in the bulk and at the Ge/Si, Ge/SiO_2, and Si/SiO_2 interfaces are incorporated into the measured noise response (see the supplementary material for reverse-bias simulations of the space-charge regions). This broader contribution complicates the decoupling of individual defect mechanisms. A systematic reverse-bias study, while beyond the scope of the present work, remains an important direction for future research.

Typically, the current noise spectral density S_I can be parameterized via

$$S_I(f) = K\frac{I^{\beta}}{f^{\alpha}}, \tag{3}$$

where K is a normalization factor, $\alpha = -\partial \ln S_I/\partial \ln f$ is the slope of the LF noise spectrum, and β indicates the dependence on the diode current I.

Figures 4(a)–4(c) show the noise spectral density normalized by the current, S_I/I^2, for the three Ge-on-Si PDs, measured at forward voltages from 0.1 to 0.6 V, as a function of frequency at $T = 295$ K. The LF noise spectra are of the $1/f^{\alpha}$ type, with α close to 1. However, for bias of 0.2 to 0.3 V, weak Lorentzian humps can be observed. To detect more accurately the presence of peaks, replotting the data as $f \times S_I/I^2$ helps to emphasize deviations from $1/f$ power law.[63] Such plots are depicted in Figs. 4(d)–4(f). Weak and broad peaks are discernible in noise spectra at voltage levels of 0.2 to 0.3 V, most notably for the SLPIN-D device, suggesting the presence of generation-recombination noise associated with traps having an average characteristic time constant of $\tau = 1/(2\pi f_c)$, where f_c is the corner (peak) frequency. These features become more evident in the temperature-dependent LF noise analysis presented in Sec. IV C.

The G–R noise model for p–i–n junctions describes how carrier capture and emission via bulk or interface traps within the space-charge region (SCR) induce fluctuations in local charge density. These fluctuations modulate the electric field distribution inside the SCR and, thus, create time-dependent fluctuations in the total current flowing through the diode.[44,64–66] A generalized expression for the G–R noise current spectral density originating from traps within the SCR of width W is given by[44,66]

$$S_I(f) = \int_0^W \int_{\tau_1}^{\tau_2} \left(\frac{\bar{I}}{\eta V_T}\right)^2 \left(\frac{q x_j}{A\varepsilon_0\varepsilon_s}\right)^2 \times g(\tau)\frac{4\tau}{1+((2\pi f)^2\tau^2)} N_t f_t(1-f_t)dx d\tau. \tag{4}$$

Here, $g(\tau)$ represents the distribution of trap time constants, while N_t is the total number of traps in the section $[x_j, x_{j+1}]$. $f_t(1-f_t)$ captures the bias dependence of trap occupancy, where f_t is the probability of trap occupation. The bias dependence of $f_t(1-f_t)$ arises from the relative alignment of the quasi-Fermi levels with the trap energy level E_t.[28] As the forward bias changes, it alters the carrier distributions and the position of the quasi-Fermi levels, $E_{F_{n,p}}$, thus modulating the carrier-trap coupling. This mechanism can contribute to the voltage-dependent activation or suppression of specific trap contributions to the measured LF noise spectra. Furthermore, the ideality factors η, ranging from 1.25 to 1.5 at 0.2 V and 295 K, place the junctions in a regime in which both diffusion and SRH recombination are active, which can broaden the observed G–R peak. Below and above 0.2–0.3 V, the noise originates from a broad distribution of trap time constants, leading to a superposition of Lorentzian spectra that collectively form a $1/f$-like spectrum.

To determine whether the observed broad peak components originate from discrete dominant defect states, random telegraph signal (RTS) measurements were performed at $T = 295$ K in the bias range of 0.1 to 0.3 V, analyzing current fluctuations I as a function of time t. Time-lag analysis plotting $I(t_{i+1})$ vs $I(t_i)$ was used to identify multi-level switching behavior between distinct traps.[67,68] The measurements do not show any distinguishable RTS patterns at room temperature, with no observable discrete step changes in current (see the supplementary material). Instead, the current fluctuations exhibited Gaussian distribution characteristics at all voltages, indicating that the noise originates from a statistically significant ensemble of defect states rather than isolated fluctuators. At some conditions (0.4 and 0.5 V for the SLPIN and SLPIN-D devices, 0.4 V for the VPIN devices), the curves follow a pure $1/f$ dependence, typically associated with diffusion noise. This behavior likely originates from variations in carrier scattering due to fluctuations in the charge state of defects in the quasi-neutral regions[54,69] and have the following dependency:

$$S_I(f) \propto \frac{I}{f}. \tag{5}$$

19 December 2025 09:54:34

© Author(s) 2025

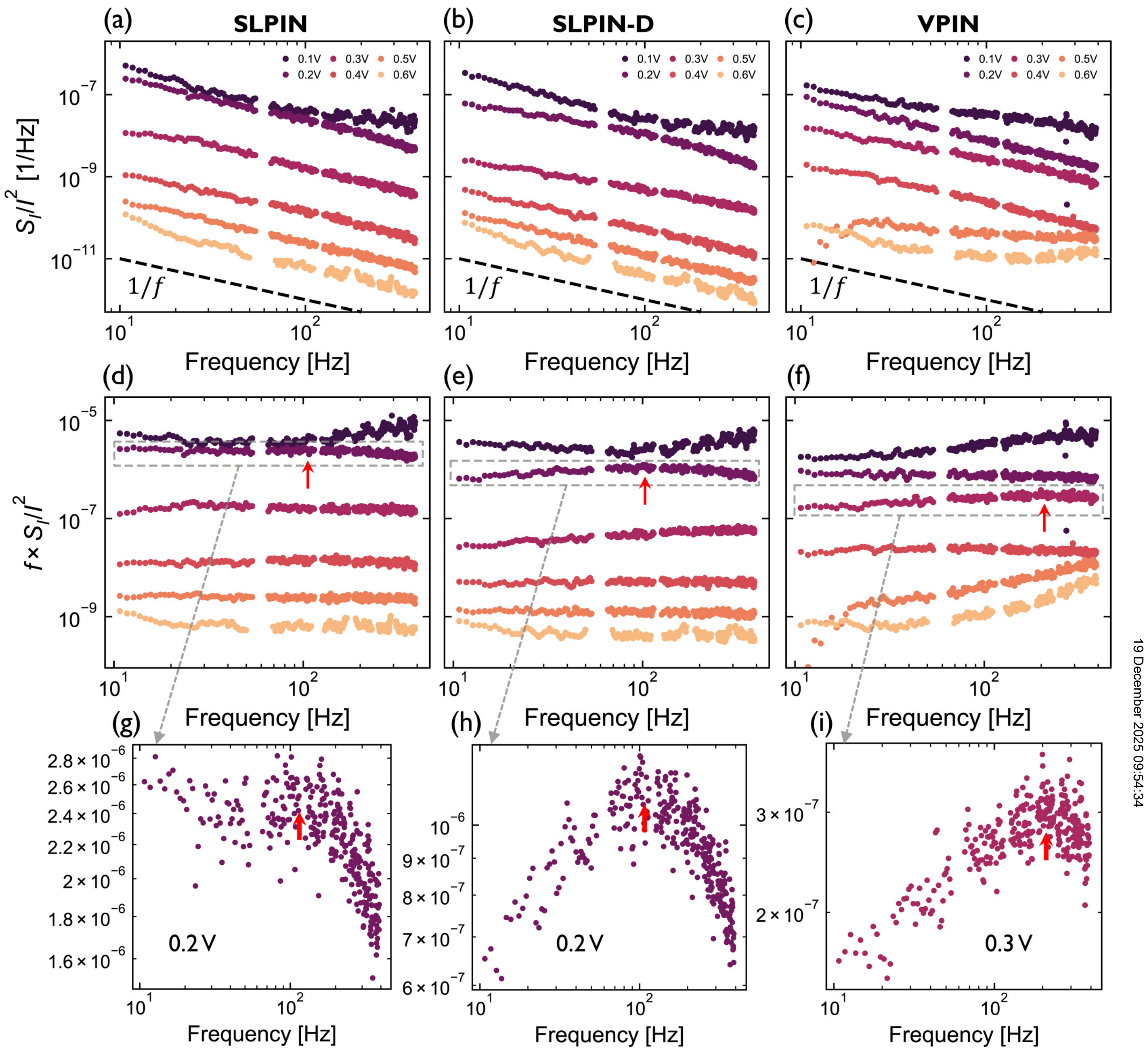

FIG. 4. The normalized current noise spectral density S_I/I^2 as a function of frequency f, measured at different forward bias voltages, at $T = 295$ K, for the (a) SLPIN, (b) SLPIN-D, and (c) VPIN devices. The normalized noise current spectral density multiplied by the frequency, $f \times S_I/I^2$, is also shown at different forward bias voltages for the (d) SLPIN, (e) SLPIN-D, and (f) VPIN devices. Panels (g)–(i) provide magnified views with red arrows highlighting the weak and broad peaks in the $f \times S_I/I^2$ spectra.

The study of noise spectral density dependence on the diode current, given by β in Eq. (3), proves to be very useful in understanding the dominant noise source in forward-biased junction devices. Figures 5(a) and 5(b) show S_I/I^2 vs V and S_I vs I, respectively, measured at $f = 50$ Hz and $T = 295$ K for the three photodiodes under study. From these plots, three distinct regimes emerge, reflecting transitions between dominant noise sources and transport mechanisms.

In the low-current regime ($V \leq 0.2$ V), the measured S_I vs I relationship closely follows a near quadratic trend $S_I \sim I^2$. This behavior is consistent with $1/f$ noise originating from defect-assisted G–R events within the depletion region,[40,44,46,47] as described by

19 December 2025 09:54:34

© Author(s) 2025

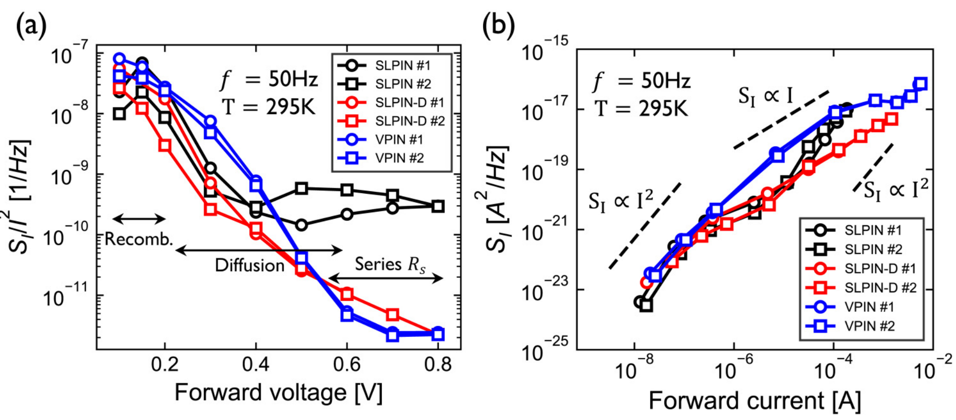

FIG. 5. (a) S_I/I^2 as a function of forward voltage V and (b) S_I as a function of forward current I, measured at $f = 50$ Hz and $T = 295$ K, for the three Ge-on-Si photodiodes.

Eq. (4). Furthermore, G–R noise associated with surface states in p–n junctions, originating from the junction periphery or the surface of the SCR, has been shown to follow a $I^{2/\eta}$ power-law dependence.[46,70] Examining the extracted η values in Figs. 2(d)–2(f), we find $\eta \in [1.1 - 1.4]$ at room T, which corresponds to $\beta = 2/\eta \in [1.82 - 1.43]$. This implies that both bulk and interface-related traps within the space-charge region can contribute to the observed noise in the low-injection regime. In the intermediate current regime, corresponding to a voltage range of $0.2\,\mathrm{V} \leq V \leq 0.5\,\mathrm{V}$, the current dependence gradually transitions toward a linear relation with $S_I \sim I$. This transition is more pronounced in the SLPIN and SLPIN-D devices, while it appears less distinctly in the VPIN device. As described by Eq. (5), this linear dependence is characteristic of diffusion noise originating from carrier scattering and recombination in the quasi-neutral regions of p–n junctions. This change occurs at the same current levels ($I \sim 10^{-6}–10^{-5}$) where the Lorentzian hump features were observed. In systems with multiple trap levels, the G–R noise spectra are governed by the spatial distribution and occupancy states of active traps, as well as the relative position of these traps with respect to the position of Fermi levels throughout the depletion regions, which can experience significant modification with increasing forward bias voltage. Finally, in the high-current regime ($V \geq 0.5\,\mathrm{V}$), the diode current will start to be influenced by the series resistance R_s. Typically, the $1/f$ noise due to fluctuations in resistive elements follows a quadratic current dependence $S_I \sim I^2$,[71] which is observed for SLPIN and VPIN devices.

TCAD simulations were performed to study the space-charge region dynamics in these photodiode architectures and understand the role of the defect-rich Ge/Si interface, otherwise inaccessible by measurements presented in Figs. 4 and 5. Figure 6 shows the simulated electric field distributions for both SLPIN and VPIN structures at room temperature under a forward bias of 0.2 V. The SLPIN-D simulations are not shown because the SCR characteristics and the noise-sensitive depletion regions are closely similar to the SLPIN devices (see the supplementary material for SLPIN-D simulation data). For the VPIN device, only the left-part of the device is shown due to its symmetry. The dominant current conduction pathways through the lateral p-Si/i-Ge/n-Si (SLPIN) and the vertical p$^+$Ge/i-Ge/n-Si (VPIN) heterojunctions are indicated by white arrows (see the supplementary material for current density plots). Additionally, schematic representations of the expected Ge/Si interface defects and bulk threading dislocations near the heterojunction interface are included. The approximate

19 December 2025 09:54:34

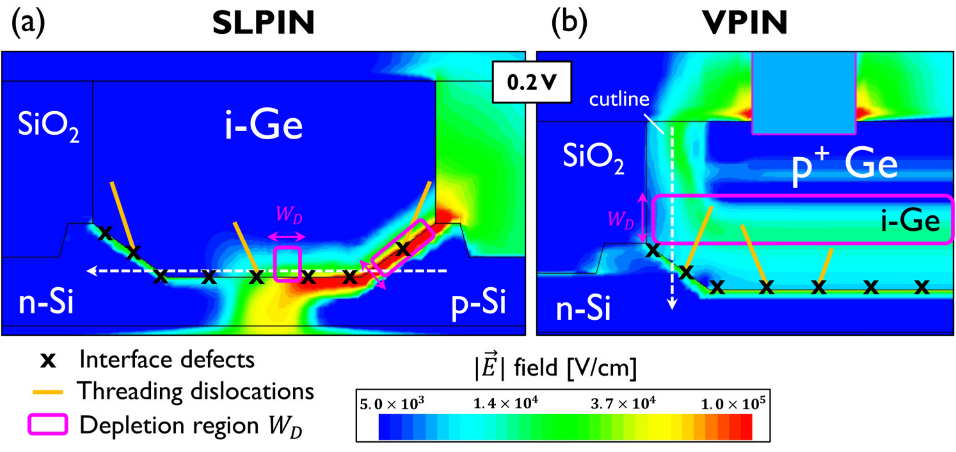

FIG. 6. Simulated electric field profiles at $T = 295$ K under 0.2 V forward bias for (a) SLPIN and (b) VPIN devices. Schematic representations of interface defects and threading dislocations are overlaid on the field plots. The approximate boundaries of depletion regions, which serve as active areas for G–R noise mechanisms, are indicated by pink lines.

© Author(s) 2025

depletion regions at 0.2 V forward bias are also shown. We observe that the depletion regions in the SLPIN device are tightly confined near the bottom i-Ge/p-Si interface, near the high-field region. The presence of high fields originates from the strong valence band offset occurring at this interface. The additional p^+ and n^+ doping in SLPIN-D devices enhances the electric field near the top i-Ge/SiO_2 interface. This in turn increases their susceptibility to dark current degradation under electro-thermal stress.[24] This additional doping has minimal impact on the space-charge region near the bottom i-Ge/p-Si interface, thereby explaining the similar LF noise behavior in SLPIN and SLPIN-D devices. In contrast, the VPIN structure exhibits a broader depletion region located within the i-Ge layer, spatially separated from the i-Ge/n-Si interface. These results provide insight into locations of the G–R noise centers, indicating that traps near the Ge/Si interface dominate in lateral devices, whereas vertical devices are more sensitive to bulk Ge traps.

In Fig. 7, the energy band diagrams are visualized along the dominant current injection pathways (depicted in Fig. 6) at forward bias conditions of 0.2 and 0.4 V. In the SLPIN device, the electrons flow from the i-Ge layer toward the p-Si interface. Assuming traps located near the midgap energy, carrier recombination can occur both within the i-Ge depletion region and at the i-Ge/p-Si heterojunction interface. In practice, a broad distribution of trap energy levels is likely, particularly at the heterointerface, as schematically represented in the band diagrams. As described by Eq. (4), the G–R noise magnitude reaches a maximum when the trap energy aligns with the local quasi-Fermi level and decays rapidly for energy separations exceeding a few k_BT. As the forward bias increases, two key mechanisms influence the noise behavior. First, an increase of V can modify and strongly reduce the spatially distributed difference $E_t - E_F$ inside the junction. This reduces the effective number of traps in resonance with the Fermi level, thus reducing G–R noise magnitude. In addition, at higher V, the junction barrier height is reduced and a decrease of W_D is observed in

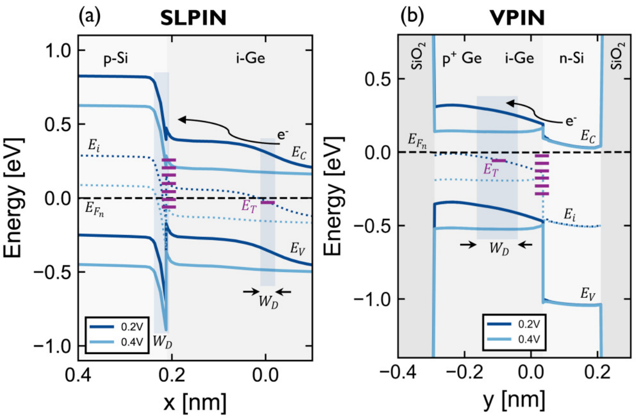

FIG. 7. Simulated energy band diagram of the Ge/Si heterojunctions in (a) SLPIN and (b) VPIN devices, extracted at $T = 295$ K for two forward bias voltages (0.2 and 0.4 V). Schematic representations of interface and bulk defect states within the bandgap are overlaid on the plots in purple.

the i-Ge layer, facilitating the diffusion of carriers across the junction and leading to enhanced diffusion noise in the quasi-neutral regions. However, the W_D around the i-Ge/p-Si interface is weakly reduced due to the large valence band offset. This suggests that the G–R contribution in the SLPIN device may originate from traps located near the bottom i-Ge layer, close to the Ge/Si heterojunction.

In the VPIN device, the electrons flow from the n-Si layer toward the p^+ Ge layer. Here, at 0.2 V, the W_D region is localized within the i-Ge layer, further away from the Ge/Si heterointerface, but laterally adjacent to the Ge/SiO_2 interface. At higher voltage, a notable reduction of the junction barrier is observed, as well as a shift of the $E_t - E_F$ alignment inside the junction. Unlike the SLPIN structure, the VPIN's wider and more symmetrically distributed depletion region, located away from the Ge/Si heterojunction, appears to average out localized defect effects over a broader bulk volume. This spatial smoothing likely contributes to the more gradual evolution of the ideality factor η and the current exponent β with bias.

C. Temperature dependence of LF noise

The LF noise measurements were performed in the temperature range from 240 to 360 K at a forward bias voltage of 0.2 V to capture the evolution of the spectra in the recombination-dominated charge transport regime of interest. Figures 8(a)–8(c) show S_I/I^2 vs f, at multiple temperatures for the three different Ge-on-Si photodiodes. Figures 8(d)–8(f) replot the data as $f \times S_I/I^2$ vs f to make the G–R peak more visible. Broad peaks can be observed for the SLPIN and SLPIN-D in the studied frequency range at some specific temperatures. As the temperature increases, f_c tends to shift to a higher frequency. The presence of peaks is less visible for the VPIN device. As the temperature increases, the thermally activated carrier capture and emission rates from traps accelerate, resulting in shorter characteristic time constants and shift of f_c to higher frequencies. Furthermore, a notable trend emerges in the characteristic frequency slope α, which systematically decreases with increasing temperature. When α deviates significantly from 1.0, this indicates the presence of G–R recombination noise caused by specific defect centers or highly non-uniform defect-energy distributions.[36] These discrete Lorentzian G–R noise components superimpose on the underlying $1/f$ background noise, which originates from a broader ensemble of less dominant defect states. Figure 9 shows the temperature dependence of α, extracted at $f = 50$ Hz, for all three devices. The spectral slope demonstrates a consistent pattern: values (between 1.4 and 1.7 at 240 K) decreasing monotonically with increasing temperature before saturating at values between 0.75 and 1.0 for temperatures above 300 K. The transition is sharper for the SLPIN and SLPIN-D devices, compared to the VPIN device. This behavior suggests a transition in the dominant noise mechanisms around 300 K: G–R noise from few dominant traps at low temperature, toward diffusion-limited noise in the quasi-neutral regions at higher temperature.

Figure 10 shows S_I/I^2 as a function of temperature T at 0.2 V for selected frequencies ranging from 50 to 350 Hz. For the SLPIN and SLPIN-D devices, distinct noise peaks emerge between 280 and 300 K. As the frequency increases, the noise peak shifts slightly to higher temperatures. In contrast, the VPIN device shows

19 December 2025 09:54:34

© Author(s) 2025

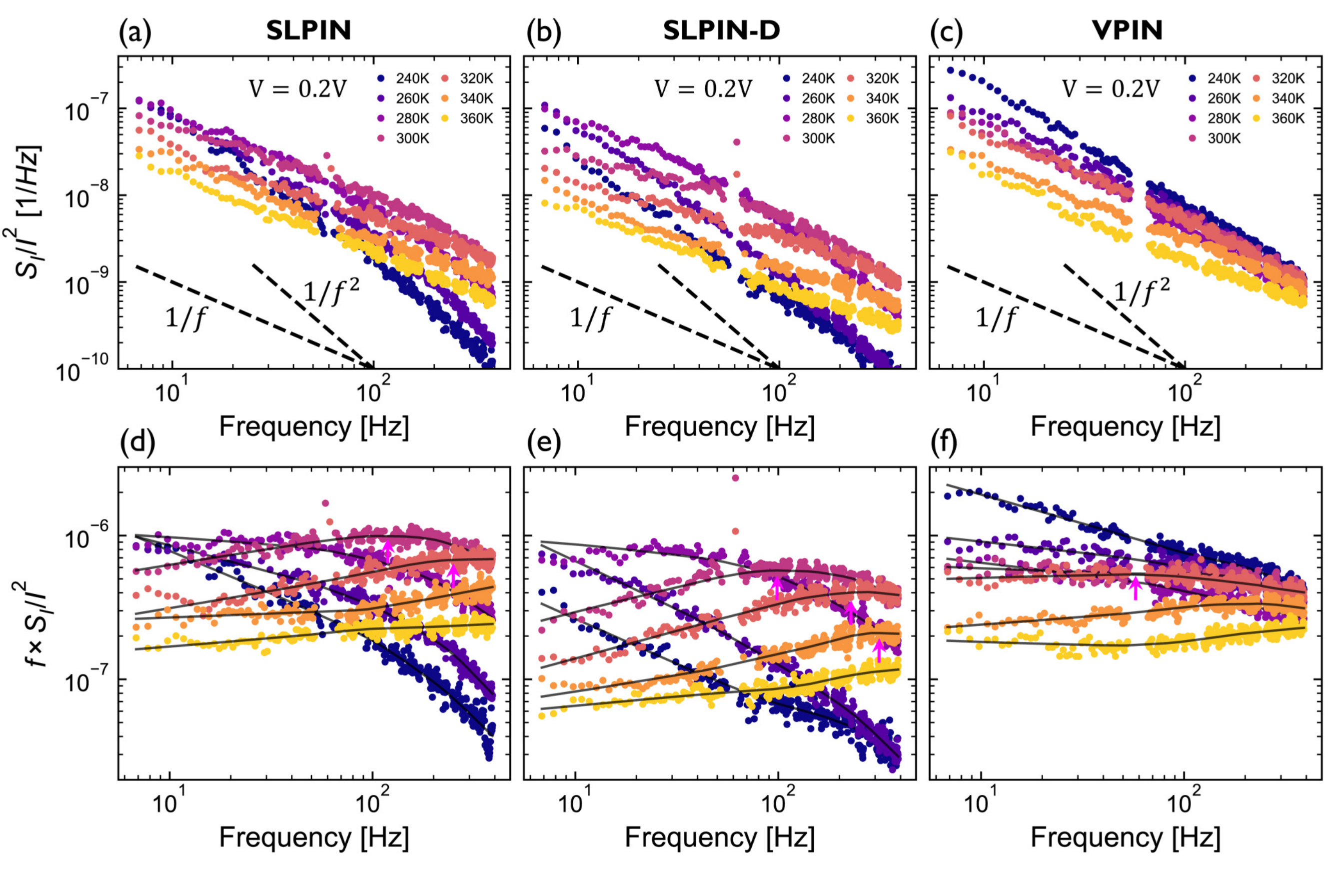

FIG. 8. The normalized noise current spectral density S_I/I^2 as a function of frequency f, measured at 0.2 V forward bias, at different temperatures, for the (a) SLPIN, (b) SLPIN-D, and (c) VPIN devices. The normalized noise current spectral density multiplied by the frequency, $f \times S_I/I^2$, measured at 0.2 V forward bias, at different temperatures, for the (d) SLPIN, (e) SLPIN-D, and (f) VPIN devices. Solid black lines show smoothed data trends for visual guidance.

19 December 2025 09:54:34

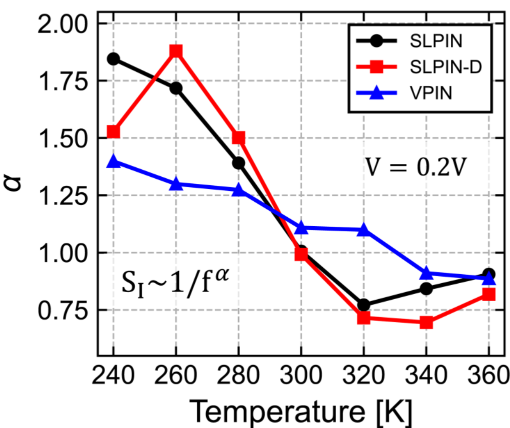

FIG. 9. The α parameter dependence on temperature for the three Ge-on-Si photodiode configurations, measured under a forward bias of 0.2 V.

significantly attenuated or absent peaks over the same temperature range. Interestingly, the noise maxima occur precisely at the transition temperature where the frequency exponent α of the noise spectrum exhibits a slope change.

The temperature dependence of $1/f$ noise was originally described by Dutta and Horn.[72] This model provides a detailed description of the effective energy distributions of defects that dominate low-frequency noise in metal films, microelectronic devices, and materials. However, the conventional formalism, which assumes a single thermally activated ensemble of two-state fluctuators with a stationary energy distribution and constant coupling to the measured current, cannot be applied across the full temperature range under study of the forward-biased Ge-on-Si photodiodes. As temperature increases, the dominant conduction mechanism gradually shifts from generation-recombination in the depletion region at low temperatures to diffusion-limited injection in the quasi-neutral regions at higher temperatures. Each regime is associated with different sets of active defect states, activation energies, and coupling mechanisms. As a result, applying a single Dutta–Horn analysis across the full temperature range is not possible. To get information on the defect acting on

© Author(s) 2025

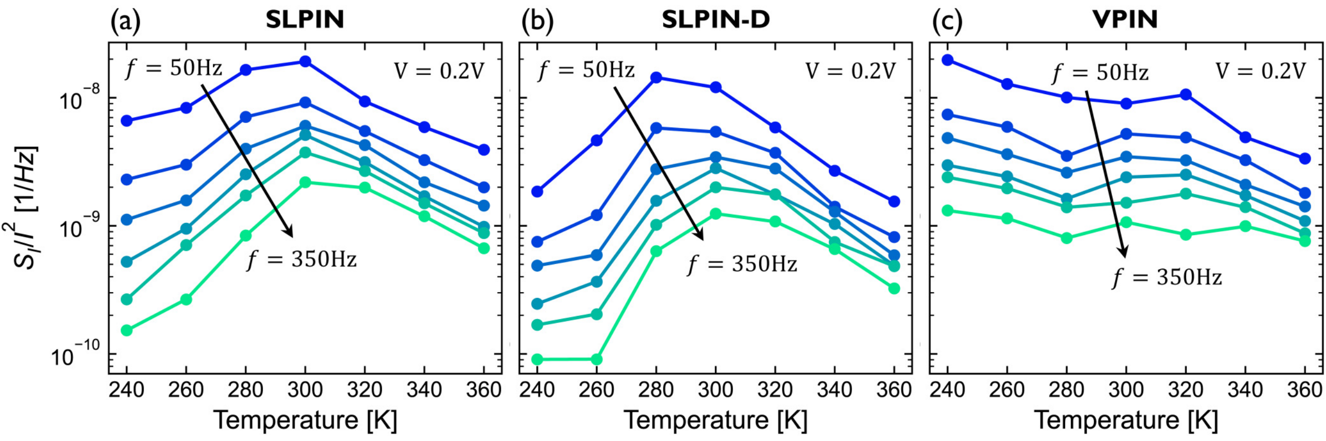

FIG. 10. Temperature dependence of the normalized current noise spectral density, S_I/I^2, measured under 0.2 V forward bias for (a) SLPIN, (b) SLPIN-D, and (c) VPIN device configurations. Data are plotted at selected frequencies ranging from 50 to 350 Hz.

the G–R noise, one must fully solve Eq. (4). This requires detailed knowledge of several spatially and thermally dependent parameters (trap densities, occupancy probabilities, electric field $\vec{E}$, and carrier distribution). In the context of Ge-on-Si photodiodes, this task is particularly challenging due to the highly non-uniform SCR.

Despite the above noted limitations, previous studies have shown that peaks in the temperature dependence of LF noise can indicate changes in material properties or shifts in the dominant transport regime.[48] In this case, structural changes are ruled out. Ge-on-Si diodes are known to be stable between 240 and 360 K, with no phase transitions or crystallographic changes observed in this range. Therefore, the observed noise behavior strongly supports the interpretation that the dominant noise source transitions from G–R noise at low temperature to diffusion noise at high temperature. The peak in S_I/I^2 marks the temperature at which all the traps in the depletion region have the highest fluctuation rates and the strongest coupling to the current. Below the peak, G–R noise dominates where fewer traps are active. The main contribution to G–R noise originates from defects located in a narrow region near the Ge/Si interface. At elevated temperatures, above the peak, the increased thermal energy leads to higher free carrier concentrations, enhancing carrier diffusion and recombination into the quasi-neutral regions. Simultaneously, the built-in potential barriers at the junction are reduced, further facilitating charge transport. In this region, the noise is dominated by mobility and scattering fluctuations in the bulk.

D. Total-ionizing-dose effects on LF noise

Total-ionizing-dose (TID) effects can provide additional information on the low-frequency noise behavior of semiconductor devices.[30,37,73,74] Figure 11 compares forward I–V characteristics for the SLPIN and SLPIN-D devices, before and after being irradiated with 10-keV x rays to a TID of 1 Mrad (SiO_2), measured in the temperature range of 240–360 K. In the low-injection regime, from 0 to 0.35 V, the DC response of the devices is significantly affected by TID irradiation. This voltage range, strongly dominated by SRH recombination within the depletion regions, exhibits an increase in the forward current at each temperature. In addition, as shown in the insets of the figure, the ideality factor at 0.2 V increased after irradiation at each temperature, indicating more pronounced recombination current contributions. Above 0.35 V, the forward conduction is dominated by diffusion of free carriers and series resistance, which were found to be not affected by TID-induced

19 December 2025 09:54:34

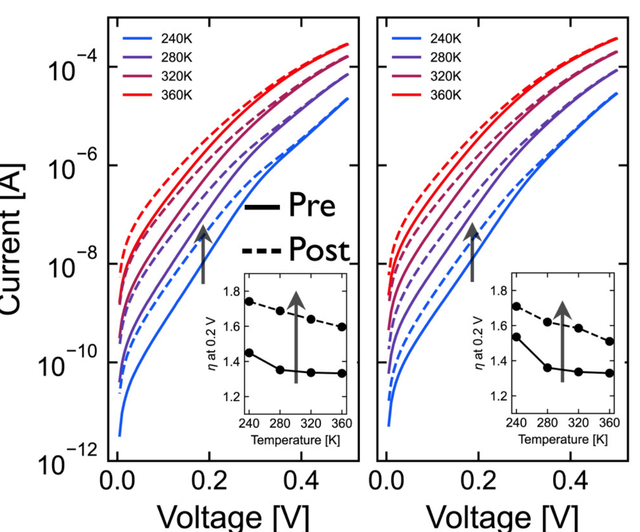

FIG. 11. Current–voltage I–V characteristics measured in forward bias between 240 and 360 K, before (continuous lines) and after (dashed lines) 10-keV x-ray irradiation to a TID of 1 Mrad (SiO_2) for the (a) SLPIN and (b) SLPIN-D devices. The insets show the ideality factor η at 0.2 V as a function of temperature, before and after TID irradiation.

© Author(s) 2025

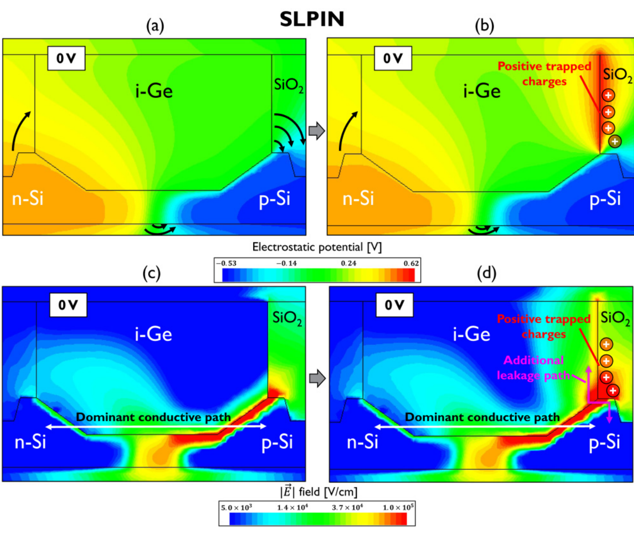

FIG. 12. Simulated (a) and (b) electrostatic potential and (c) and (d) electric field profiles at 0 V and $T = 295$ K for the SLPIN device, (a) and (c) without and (b) and (d) with positive trapped charges ($N_{ox} = 10^{12}$ cm^{-2}). Black arrows indicate the direction of $\vec{E}$. The expected trapped charge locations due to TID irradiation are overlaid on the plots, showing how trapped charges locally distort the potential and can create additional leakage paths near the active space-charge region.

degradation. Previous studies show that the dominant TID effects in these structures are caused by net positive charge trapping in oxides located near the Ge/SiO_2 and Si/SiO_2 interfaces,[75–78] affecting the electrostatics of the space-charge region.[79] This, in turn, can lead to potential barrier lowering, local enhancement of the electric field and SRH recombination rate inside the junction,[24] leading to the creation of additional current leakage paths. The exact trapped charge distribution will depend on the oxide trap densities, defect properties, electric field magnitudes, and electrostatic potential distribution.[80,81] Figure 12 shows TCAD simulations of (a) the electrostatic potential and (c) the $\vec{E}$ field for the SLPIN structure at 0 V and 295 K before irradiation, mimicking the conditions experienced by the device under experimental irradiation (see the supplementary material for the SLPIN-D results). The simulations reveal a high $\vec{E}$ field magnitude and strong electrostatic potential gradient near the bottom i-Si/BOX interface and near the right i-Ge/SiO_2 and p-Si/SiO_2 corner interfaces. Trapped charges located at the i-Si/BOX interface are situated approximately 190 nm away from the active diode conductive path and hence will have negligible impact on the device characteristics. However, traps near the i-Ge/SiO_2 corner can locally influence the electrostatic potential and create an additional leakage path near the heterojunction. To illustrate this effect, a uniform sheet of positive trapped charges ($N_{ox} = 10^{12}$ cm^{-2}), consistent with reported values in the literature,[75,79,82,83] was placed at the right i-Ge/SiO_2 interface. The resulting potential and field maps [Figs. 12(b) and 12(d)] show a

19 December 2025 09:54:34

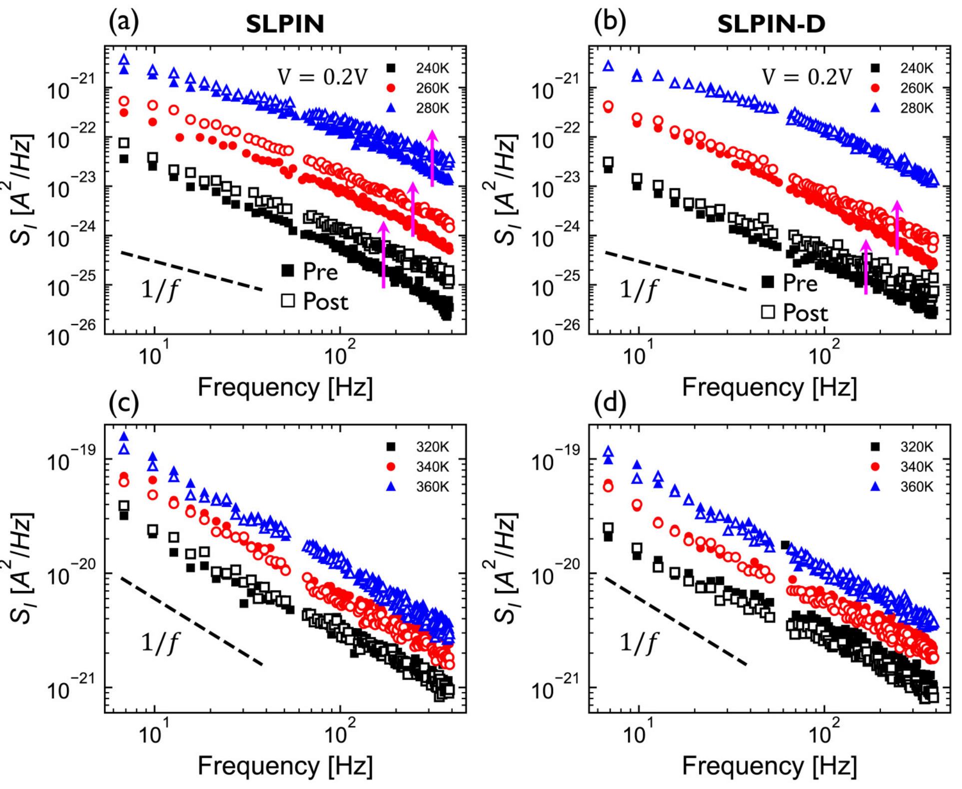

FIG. 13. The noise current spectral density S_I as a function frequency f at 0.2 V bias, measured below [(a) and (b)] and above [(c) and (d)] 300 K for the (a) and (c) SLPIN and (b) and (d) SLPIN-D devices. Solid symbols denote the as-processed devices, and open symbols denote the devices irradiated at $T = 295$ K with 10-keV x rays up to a TID of 1 Mrad (SiO_2). Increases in the noise magnitudes are only observed in the low-temperature range, below 300 K.

© Author(s) 2025

pronounced potential distortion and enhanced $\vec{E}$ field magnitude near the i-Ge/p-Si junction.

Figure 13 shows S_I vs f for the SLPIN and SLPIN-D devices before and after TID exposure. The data are separated into two temperature ranges: below 300 K [Figs. 13(a) and 13(b)] and above 300 K [Figs. 13(c) and 13(d)]. At lower temperatures, the noise magnitude increases after TID irradiation, while the spectral shape (and consequently the α slope) remains largely unchanged. This behavior indicates that x-ray irradiation has activated additional trap centers participating in the G–R noise at low temperature. However, the nature of the new generated traps remains unchanged, meaning that no new trap types were created within the junction during TID. A possible explanation is that TID alters the electrostatic potential landscape, modifying the trap occupancy probability f_t and thereby enhancing recombination activity at existing defect states, without introducing new trap types or energy levels in the SCR. At elevated temperatures, above 300 K, the noise spectra remain relatively unaffected by TID irradiation. This reflects that bulk diffusion noise, governed by carrier scattering and mobility fluctuations in this temperature range, is less affected by electrostatic potential modifications due to interface trapped charges.

In addition, Fig. 14 depicts the normalized S_I/I^2 vs f for the SLPIN and SLPIN-D devices before and after TID exposure. Interestingly, a strong decrease in normalized current noise is observed in the whole temperature range. This overall behavior suggests that TID-induced degradation facilitates the reduction of the junction barrier and provides additional conduction channels, boosting significantly the DC forward current I.[14] However, TID minimally enhances the noise S_I where generation-recombination dominates. The net result is that S_I/I^2 drops at all temperatures. These findings highlight that the mechanisms governing the DC current conduction and the low-frequency noise response in Ge-on-Si p–i–n photodiodes can be fundamentally different. This decoupling between forward conduction and noise generation mechanisms enables understanding of the physics of Ge-based photodiodes and can be helpful to assessments of interface material quality.

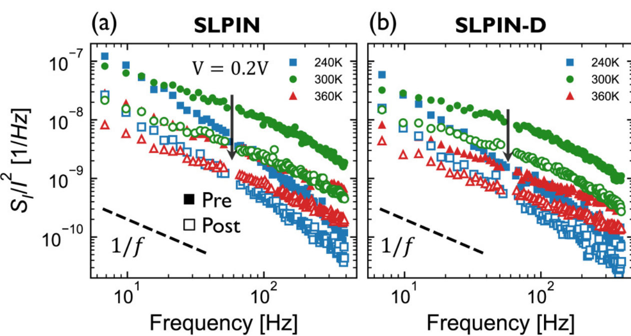

FIG. 14. The normalized current noise spectral density, S_I/I^2, as a function of frequency f measured at 0.2 V forward bias, at three different temperatures, before (solid symbols) and after (open symbols) 10-keV x-ray irradiation to a TID of 1 Mrad (SiO_2) for the (a) SLPIN and (b) SLPIN-D devices.

V. SUMMARY AND CONCLUSIONS

In summary, we reported on the forward bias voltage and temperature dependence of the low-frequency $1/f$ noise in three waveguide-integrated Ge-on-Si p–i–n photodiode architectures: doped-Si lateral (SLPIN), doped-Ge and doped-Si lateral (SLPIN-D), and vertical (VPIN) heterojunctions. Forward I–V characteristics reveal mixed-mode conduction comprising Shockley–Read–Hall (SRH) recombination and diffusion currents in the low-injection regime, with relative contributions varying with temperature. Voltage-dependent noise measurements exhibit broad generation-recombination (G–R) Lorentzian peaks near 0.2 V bias, near the transition voltage from G–R-dominated to diffusion-limited current noise. Our TCAD simulations demonstrate that the lateral devices exhibit pronounced G–R noise signatures due to strain-induced defects and trapping centers concentrated near the Ge/Si interface within the tight depletion region. In contrast, the Ge/Si interface in vertical devices lies outside the depletion region, leading to a noise response dominated by bulk Ge traps. Temperature-dependent $1/f$ measurements reveal a systematic evolution from G–R noise mechanisms below 300 K to diffusion-dominated noise at elevated temperature. Notably, lateral devices display non-monotonic normalized noise magnitude with a peak near 300 K, indicating a critical transition temperature where competing noise mechanisms have the strongest coupling to the current. For lateral devices, post-total-ionizing-dose (TID) irradiation analysis reveals a modest increase in the low-temperature noise magnitude ascribed to trap activation within the space-charge region. A substantial increase in forward current across all temperatures highlights the predominant effect of radiation-induced degradation on the creation of a leakage path near the interfaces. This study demonstrates how low-frequency noise analysis can support reliability assessments by linking temperature, bias, and radiation effect dependencies to the activity of critical traps in Ge-on-Si photodiodes.

19 December 2025 09:54:34

SUPPLEMENTARY MATERIAL

The supplementary material provides data supporting the conduction mechanism analysis in the reverse-bias regime, detailed random telegraph signal (RTS) measurements under forward bias, and additional TCAD simulation parameters and results.

ACKNOWLEDGMENTS

The imec industrial affiliation R&D program on Optical I/O is acknowledged for technical support. Sharon M. Weiss, Tianfang K. Liu, Phoenix Harris, and Xuyi Luo are acknowledged for experimental and technical support. Emmanuel Chery, Steven L. Kosier, and Enxia Zhang are thanked for insightful technical discussions. This work was supported by a grant for a long stay abroad from the Research Foundation—Flanders (FWO, Belgium) (Application No. #V439524N) and by the National Science Foundation (NSF, USA) Industry-University Cooperative Research (IUCRC) Electronic-Photonic Integrated Circuits for Aerospace (EPICA) (Award No. 2052742). Kellen P. Arnold's effort on this work was supported by the National Aeronautics and Space Administration

© Author(s) 2025

(NASA) Space Technology Graduate Research Opportunities (NSTGRO) 2023 Fellowship under Award No. 80NSSC23K1198.

AUTHOR DECLARATIONS

Conflict of Interest

The authors have no conflicts to disclose.

Author Contributions

Solomon Musibau: Conceptualization (lead); Formal analysis (lead); Investigation (lead); Methodology (lead); Software (lead); Writing – original draft (lead); Writing – review & editing (lead). **Kellen P. Arnold:** Conceptualization (supporting); Formal analysis (supporting); Funding acquisition (supporting); Investigation (supporting); Methodology (supporting); Resources (supporting); Writing – review & editing (supporting). **Anurag R. Veluri:** Formal analysis (supporting); Investigation (supporting); Methodology (supporting); Resources (supporting); Writing – review & editing (supporting). **Jacopo Franco:** Conceptualization (equal); Formal analysis (equal); Funding acquisition (supporting); Investigation (equal); Methodology (equal); Project administration (supporting); Supervision (equal); Writing – review & editing (equal). **Artemisia Tsiara:** Formal analysis (supporting); Funding acquisition (supporting); Methodology (supporting); Project administration (supporting); Resources (lead); Supervision (supporting); Writing – review & editing (supporting). **Kristof Croes:** Funding acquisition (supporting); Project administration (supporting); Resources (supporting); Supervision (supporting). **Joris Van Campenhout:** Funding acquisition (supporting); Project administration (supporting); Resources (supporting). **Ronald D. Schrimpf:** Formal analysis (supporting); Funding acquisition (supporting); Methodology (supporting); Project administration (supporting); Resources (supporting); Supervision (supporting); Validation (supporting); Writing – review & editing (supporting). **Robert A. Reed:** Formal analysis (supporting); Funding acquisition (lead); Investigation (supporting); Methodology (supporting); Project administration (supporting); Resources (supporting); Supervision (supporting); Validation (supporting); Writing – review & editing (supporting). **Ingrid De Wolf:** Funding acquisition (supporting); Project administration (supporting); Supervision (supporting); Validation (supporting); Writing – review & editing (supporting). **Daniel M. Fleetwood:** Conceptualization (supporting); Formal analysis (supporting); Funding acquisition (supporting); Investigation (supporting); Methodology (supporting); Resources (supporting); Supervision (lead); Validation (lead); Writing – review & editing (lead).

DATA AVAILABILITY

The data that support the findings of this study are available from the corresponding author upon reasonable request.

REFERENCES

[1]P. Absil, K. Croes, A. Lesniewska, P. De Heyn, Y. Ban, B. Snyder, J. De Coster, F. Fodor, V. Simons, S. Balakrishnan, G. Lepage, N. Golshani, S. Lardenois, S. A. Srinivasan, H. Chen, W. Vanherle, R. Loo, R. Boufadil, M. Detalle, A. Miller, P. Verheyen, M. Pantouvaki, and J. Van Campenhout, in *2017 IEEE International Electron Devices Meeting (IEDM)* (IEEE, 2017), pp. 34.2.1–34.2.4.
[2]N. Margalit, C. Xiang, S. M. Bowers, A. Bjorlin, R. Blum, and J. E. Bowers, Appl. Phys. Lett. **118**, 220501 (2021).
[3]Y. Shi, Y. Zhang, Y. Wan, Y. Yu, Y. Zhang, X. Hu, X. Xiao, H. Xu, L. Zhang, and B. Pan, Photonics Res. **10**, A106 (2022).
[4]R. Mahajan, X. Li, J. Fryman, Z. Zhang, S. Nekkanty, P. Tadayon, J. Jaussi, S. Shumarayev, A. Agrawal, S. Jadhav, K. A. Singh, A. Alduino, S. Gujjula, C.-P. Chiu, T. Nordstog, K. J. Hosseini, S. Sane, N. Deshpande, K. Aygun, A. Sarkar, P. Dobriyal, S. Pothukuchi, V. Pogue, and D. Hui, J. Lightwave Technol. **40**, 379 (2022).
[5]F. J. Ferraro, P. De Heyn, M. Kim, N. Rajasekaran, M. Berciano, G. Muliuk, D. Bode, G. Lepage, S. Janssen, R. Magdziak, J. De Coster, H. Kobbi, S. Lardenois, N. Golshani, L. Shiramin, C. Marchese, S. Rajmohan, S. Nadarajan, N. Singh, S. Radhakrishnan, A. Tsiara, P. Xu, A. Karagoz, D. Yudistira, M. Martire, A. Shahar, M. Chakrabarti, D. Velenis, W. Guo, A. Miller, K. Croes, S. Balakrishnan, P. Verheyen, Y. Ban, J. Van Campenhout, and P. P. Absil, Proc. SPIE **12429**, 1242909 (2023).
[6]M. M. P. Fard, G. Cowan, and O. Liboiron-Ladouceur, Opt. Express **24**, 27738 (2016).
[7]H. Chen, P. Verheyen, P. De Heyn, G. Lepage, J. De Coster, S. Balakrishnan, P. Absil, G. Roelkens, and J. Van Campenhout, J. Appl. Phys. **119**, 213105 (2016).
[8]L. Virot, D. Benedikovic, B. Szelag, C. Alonso-Ramos, B. Karakus, J.-M. Hartmann, X. Le Roux, P. Crozat, E. Cassan, D. Marris-Morini, C. Baudot, F. Boeuf, J.-M. Fédéli, C. Kopp, and L. Vivien, Opt. Express **25**, 19487 (2017).
[9]H. Chen, M. Galili, P. Verheyen, P. De Heyn, G. Lepage, J. De Coster, S. Balakrishnan, P. Absil, L. Oxenlowe, J. Van Campenhout, and G. Roelkens, J. Lightwave Technol. **35**, 722 (2017).
[10]S. Lischke, A. Peczek, J. S. Morgan, K. Sun, D. Steckler, Y. Yamamoto, F. Korndörfer, C. Mai, S. Marschmeyer, M. Fraschke, A. Krüger, A. Beling, and L. Zimmermann, Nat. Photonics **15**, 925 (2021).
[11]G. Chen, Y. Yu, Y. Shi, N. Li, W. Luo, L. Cao, A. J. Danner, A.-Q. Liu, and X. Zhang, Laser Photonics Rev. **16**, 2200117 (2022).
[12]G. N. Tzintzarov, S. G. Rao, and J. D. Cressler, Photonics **8**, 131 (2021).
[13]L. Olanterä, C. Scarcella, M. Lalović, S. Détraz, A. Pandey, T. Prousalidi, U. Sandven, C. Sigaud, C. Soós, and J. Troska, IEEE Trans. Nucl. Sci. **71**, 728 (2024).
[14]K. P. Arnold, S. Musibau, H. M. Dattilo, H. J. Sutton, S. L. Frankowski, M. Berciano, E. X. Zhang, M. W. McCurdy, M. L. Crespillo, K. Hattar, A. Tsiara, D. Linten, K. Croes, J. V. Campenhout, R. D. Schrimpf, D. M. Fleetwood, R. A. Reed, and S. M. Weiss, IEEE Trans. Nucl. Sci. **72**, 1181 (2025).
[15]G. Terrasanta, M. Ziarko, N. Bergamasco, M. Poot, and J. Poliak, Int. J. Satell. Commun. Netw. **43**, 210 (2025).
[16]E. H. Poindexter and P. J. Caplan, Prog. Surf. Sci. **14**, 201 (1983).
[17]*Extended Defects in Germanium*, Springer Series in Materials Science, edited by C. Claeys and E. Simoen (Springer Berlin Heidelberg, Berlin, 2009), Vol. 118.
[18]M. Houssa, E. Chagarov, and A. Kummel, MRS Bull. **34**, 504 (2009).
[19]A. Stesmans, P. Somers, and V. V. Afanas'ev, J. Phys.: Condens. Matter **21**, 122201 (2009).
[20]A. Lesniewska, S. A. Srinivasan, J. Van Campenhout, B. J. O'Sullivan, and K. Croes, in *2019 IEEE International Reliability Physics Symposium (IRPS)* (IEEE, 2019), Vol. 2019, pp. 211–217.
[21]F. Sy, Q. Rafhay, J. Poette, G. Grosa, G. Beylier, P. Grosse, D. Roy, and J.-E. Broquin, IEEE Trans. Device Mater. Reliab. **19**, 688 (2019).
[22]S. Rauch, D. Lee, A. Vert, L. Jiang, and B. Min, in *2020 Optical Fiber Communications Conference and Exhibition (OFC)* (Optica, 2020), paper W2A.5.
[23]K. Croes, V. Simons, B. Truijen, P. Roussel, K. Van Sever, A. Tsiara, J. Franco, and P. Absil, in *2022 Optical Fiber Communications Conference and Exhibition (OFC)* (Optica, 2022), pp. 1–3.
[24]S. Musibau, N. Poumpouridis, A. Tsiara, J. Franco, M. Berciano, J. Van Campenhout, I. De Wolf, and K. Croes, in *2024 IEEE International Reliability Physics Symposium (IRPS)* (IEEE, 2024), pp. 41–50.

19 December 2025 09:54:34

© Author(s) 2025

[25]S. A. Srinivasan, M. Pantouvaki, S. Gupta, H. T. Chen, P. Verheyen, G. Lepage, G. Roelkens, K. Saraswat, D. V. Thourhout, P. Absil, and J. V. Campenhout, J. Lightwave Technol. **34**, 419 (2016).
[26]A. Kandeel, G. Hiblot, C. Porret, S. A. Srinivasan, Y. Shimura, R. Loo, M. Berciano, C.-K. N. Tseng, D. Malik, A. Milenin, D. Yudistira, S. Balakrishnan, A. Shahin, J. R. Vaskasi, P. Verheyen, M. Pantouvaki, M. Chakrabarti, D. Velenis, F. Ferraro, Y. Ban, D. Van Thourhout, and J. Van Campenhout, J. Lightwave Technol. **43**, 2794 (2025).
[27]A. Tsiara, M. Berciano, D. Yudistira, R. Loo, S. Musibau, P. Verheyen, F. Ferraro, Y. Ban, K. Croes, and J. Van Campenhout, in *49th European Conference and Exhibition on Optical Communication (ECOC 2023), IET Conference Proceedings*, (IET, 2023), Vol. 839, p. 1170.
[28]F. Scholz, J. M. Hwang, and D. K. Schroder, Solid State Electron. **31**, 205 (1988).
[29]L. K. J. Vandamme, IEEE Trans. Electron Devices **41**, 2176 (1994).
[30]D. M. Fleetwood, T. L. Meisenheimer, and J. H. Scofield, IEEE Trans. Electron Devices **41**, 1953 (1994).
[31]D. Ursutiu and B. K. Jones, Semicond. Sci. Technol. **11**, 1133 (1996).
[32]E. Simoen and C. Claeys, Semicond. Sci. Technol. **14**, R61 (1999).
[33]J. Xu, D. Abbott, and Y. Dai, Microelectron. J. **31**, 497 (2000).
[34]X. Y. Chen, A. Pedersen, and A. D. van Rheenen, Microelectron. Reliab. **41**, 105 (2001).
[35]S. Bychikhin, D. Pogany, L. K. J. Vandamme, G. Meneghesso, and E. Zanoni, J. Appl. Phys. **97**, 123714 (2005).
[36]D. M. Fleetwood, IEEE Trans. Nucl. Sci. **62**, 1462 (2015).
[37]D. M. Fleetwood, IEEE Trans. Nucl. Sci. **67**, 1216 (2020).
[38]G. Landi, S. Pagano, H. C. Neitzert, C. Mauro, and C. Barone, Energies **16**, 1296 (2023).
[39]V. G. Bozhkov and D. Ju. Kuzyakov, J. Appl. Phys. **92**, 4502 (2002).
[40]S. Ghosh, D. H. Mudiyanselage, S. Rumyantsev, Y. Zhao, H. Fu, S. Goodnick, R. Nemanich, and A. A. Balandin, Appl. Phys. Lett. **122**, 212109 (2023).
[41]T. G. M. Kleinpenning, J. Vac. Sci. Technol. A **3**, 176 (1985).
[42]E. Simoen, J. Vanhellemont, A. L. P. Rotondaro, and C. Claeys, Semicond. Sci. Technol. **10**, 1002 (1995).
[43]D. V. Kuksenkov, H. Temkin, A. Osinsky, R. Gaska, and M. A. Khan, Appl. Phys. Lett. **72**, 1365 (1998).
[44]F.-C. Hou, G. Bosman, E. Simoen, J. Vanhellemont, and C. Claeys, IEEE Trans. Electron Devices **45**, 2528 (1998).
[45]S. L. Rumyantsev, A. P. Dmitriev, M. E. Levinshtein, D. Veksler, M. S. Shur, J. W. Palmour, M. K. Das, and B. A. Hull, J. Appl. Phys. **100**, 064505 (2006).
[46]R. M. Todi, S. Sonde, E. Simoen, C. Claeys, and K. B. Sundaram, Appl. Phys. Lett. **90**, 2005 (2007).
[47]S. Ghosh, K. Fu, F. Kargar, S. Rumyantsev, Y. Zhao, and A. A. Balandin, Appl. Phys. Lett. **119**, 243505 (2021).
[48]S. Ghosh, D. H. Mudiyanselage, F. Kargar, Y. Zhao, H. Fu, and A. A. Balandin, Adv. Electron. Mater. **10**, 2300501 (2024).
[49]C. Li, H. Liu, J. Wang, D. Guo, B. Chen, and J. Wu, IEEE J. Quantum Electron. **60**, 4000305 (2024).
[50]L. Colace, A. Scacchi, and G. Assanto, in *8th IEEE International Conference on Group IV Photonics* (IEEE, 2011), pp. 290–292.
[51]Z. Tu, Z. Zhou, and X. Wang, IEEE J. Sel. Top. Quantum Electron. **20**, 3800306 (2014).
[52]S.-H. Chen, P.-Y. Fu, A. Tsiara, M. Van De Peer, M. Simicic, S. Musibau, Y. Ban, K.-H. Kao, W.-C. Chen, K. Serbulova, J. Van Campenhout, P. Absil, and K. Croes, in *2024 46th Annual EOS/ESD Symposium (EOS/ESD)* (IEEE, 2024), pp. 103–109.
[53]M. J. Deen, S. Rumyantsev, R. Bashir, and R. Taylor, J. Appl. Phys. **84**, 625 (1998).
[54]X. Luo, J. Montes, S. D. Koukourinkova, B. L. Vaandrager, E. S. Bielejec, G. Vizkelethy, R. D. Schrimpf, D. M. Fleetwood, and E. X. Zhang, IEEE Trans. Nucl. Sci. **71**, 591 (2024).
[55]J. Chen, Y. S. Puzyrev, R. Jiang, E. X. Zhang, M. W. McCurdy, D. M. Fleetwood, R. D. Schrimpf, S. T. Pantelides, A. R. Arehart, S. A. Ringel, P. Saunier, and C. Lee, IEEE Trans. Nucl. Sci. **62**, 2423 (2015).
[56]D. M. Fleetwood, IEEE Trans. Nucl. Sci. **60**, 1706 (2013).
[57]S. Sze and K. K. Ng, *Physics of Semiconductor Devices* (Wiley, 2006).
[58]R. Scheer, J. Appl. Phys. **105**, 104505 (2009).
[59]M. B. Gonzalez, E. Simoen, G. Eneman, B. De Jaeger, G. Wang, R. Loo, and C. Claeys, Microelectron. Eng. **125**, 33 (2014).
[60]A. Pizzone, S. A. Srinivasan, P. Verheyen, G. Lepage, S. Balakrishnan, and J. Van Campenhout, in *2020 IEEE Photonics Conference (IPC)* (IEEE, 2020), pp. 600–601.
[61]N. S. Grushko, A. V. Lakalin, and A. I. Somov, Semiconductors **42**, 1532 (2008).
[62]P. S. Goley, N. A. Dodds, M. Frounchi, G. N. Tzintzarov, R. N. Nowlin, and J. D. Cressler, IEEE Trans. Nucl. Sci. **67**, 296 (2020).
[63]X. Y. Luo, A. O'Hara, X. Li, P. F. Wang, E. X. Zhang, R. D. Schrimpf, S. T. Pantelides, and D. M. Fleetwood, J. Appl. Phys. **135**, 025702 (2024).
[64]C. T. Sah, Proc. IEEE **52**, 795 (1964).
[65]P. O. Lauritzen, IEEE Trans. Electron Devices **15**, 770 (1968).
[66]J. A. J. Tejada, A. Godoy, A. Palma, and P. Cartujo, J. Appl. Phys. **90**, 3998 (2001).
[67]E. Simoen, W. Fang, M. Aoulaiche, J. Luo, C. Zhao, and C. Claeys, Thin Solid Films **613**, 2 (2016).
[68]M. Gorchichko, E. X. Zhang, P. Wang, S. Bonaldo, R. D. Schrimpf, R. A. Reed, D. Linten, J. Mitard, and D. M. Fleetwood, IEEE Trans. Nucl. Sci. **68**, 687 (2021).
[69]T. G. M. Kleinpenning, IEEE Trans. Electron Devices **41**, 1981 (1994).
[70]A. Van der Ziel, Physica **48**, 242 (1970).
[71]D. M. Fleetwood, Nanoscale **15**, 12175 (2023).
[72]P. Dutta and P. M. Horn, Rev. Mod. Phys. **53**, 497 (1981).
[73]S. Bonaldo and D. M. Fleetwood, Appl. Phys. Lett. **122**, 173508 (2023).
[74]D. M. Fleetwood, E. X. Zhang, R. D. Schrimpf, S. T. Pantelides, and S. Bonaldo, IEEE Trans. Nucl. Sci. **71**, 555 (2024).
[75]J. R. Schwank, M. R. Shaneyfelt, D. M. Fleetwood, J. A. Felix, P. E. Dodd, P. Paillet, and V. Ferlet-Cavrois, IEEE Trans. Nucl. Sci. **55**, 1833 (2008).
[76]S. A. Francis, C. X. Zhang, E. X. Zhang, D. M. Fleetwood, R. D. Schrimpf, K. F. Galloway, E. Simoen, J. Mitard, and C. Claeys, IEEE Trans. Nucl. Sci. **59**, 735 (2012).
[77]C. X. Zhang, S. A. Francis, E. X. Zhang, D. M. Fleetwood, R. D. Schrimpf, K. F. Galloway, E. Simoen, J. Mitard, and C. Claeys, IEEE Trans. Nucl. Sci. **58**, 764 (2011).
[78]E. X. Zhang, D. M. Fleetwood, J. A. Hachtel, C. Liang, R. A. Reed, M. L. Alles, R. D. Schrimpf, D. Linten, J. Mitard, M. F. Chisholm, and S. T. Pantelides, IEEE Trans. Nucl. Sci. **64**, 226 (2017).
[79]S. Musibau, K. P. Arnold, A. R. Veluri, A. Tsiara, J. Franco, K. Croes, D. Linten, J. Van Campenhout, S. M. Weiss, R. D. Schrimpf, D. M. Fleetwood, S. L. Kosier, I. De Wolf, and R. A. Reed, "Fundamental mechanisms of total-ionizing-dose degradation in waveguide-coupled germanium-on-silicon p-i-n photodiodes," IEEE Trans. Nucl. Sci. (in press) (2026).
[80]T. R. Oldham and F. B. McLean, IEEE Trans. Nucl. Sci. **50**, 483 (2003).
[81]M. Turowski, A. Raman, and R. D. Schrimpf, IEEE Trans. Nucl. Sci. **51**, 3166 (2004).
[82]S. Bonaldo, T. Wallace, H. Barnaby, G. Borghello, G. Termo, F. Faccio, D. M. Fleetwood, S. Mattiazzo, M. Bagatin, A. Paccagnella, and S. Gerardin, IEEE Trans. Nucl. Sci. **71**, 427 (2024).
[83]S. Bonaldo, G. Borghello, F. Faccio, M. Bagatin, S. Mattiazzo, and S. Gerardin, IEEE Trans. Nucl. Sci. **72**, 2264 (2025).

19 December 2025 09:54:34

© Author(s) 2025